

Revealing high- z *Fermi*–LAT BL Lacs using *Swift* and SARA data with photometric analysis

Y. SHENG,¹ M. RAJAGOPAL,¹ A. KAUR,² M. AJELLO,¹ A. DOMÍNGUEZ,³ A. RAU,⁴ S. B. CENKO,^{5,6} J. GREINER,⁴ D. H. HARTMANN,^{1,7} I. COX,¹ S. JOFFRE,¹ C. KARWIN,¹ A. McDANIEL,¹ R. SILVER,¹ AND N. TORRES-ALBA¹

¹Department of Physics and Astronomy, Clemson University, SC 29634-0978, U.S.A.^a

²Department of Astronomy and Astrophysics, 525 Davey Lab, Pennsylvania State University, University Park, PA 16802, USA

³IPARCOS and Department of EMFTEL, Universidad Complutense de Madrid, E-28040 Madrid, Spain

⁴Max-Planck-Institut für extraterrestrische Physik, Giessenbachstraße 1, D-85748 Garching, Germany

⁵Astrophysics Science Division, NASA Goddard Space Flight Center, Mail Code 661, Greenbelt, MD 20771, USA

⁶Joint Space-Science Institute, University of Maryland, College Park, MD 20742, USA

⁷Southeastern Association for Research in Astronomy (SARA), USA

Submitted to ApJ

ABSTRACT

BL Lacertae (BL Lac) objects are a subclass of blazar, distinguished by their featureless optical spectrum. The featureless spectrum presents a challenge in measuring the redshift of the BL Lacs. In this paper, we measure the redshift of BL Lacs using the photometric dropout technique. The space-based telescope *Swift* and the ground-based SARA telescopes are employed to provide magnitudes in the *uvw2*, *uvm2*, *uvw1*, *u*, *b*, *v*, *g'*, *r'*, *i'*, *z'* filters. We observe 60 BL Lacs and report reliable redshift upper limits for 41 of them. We discover three new high- z BL Lacs ($z > 1.3$) at $1.74^{+0.05}_{-0.08}$, $1.88^{+0.07}_{-0.03}$, and $2.10^{+0.03}_{-0.04}$, bringing the number of high- z BL Lacs found by this method up to 19. Discussions are made on the implications for the blazar sequence, the *Fermi* blazar divide, and the gamma-ray horizon based on an analysis of the 4LAC catalog and all high- z BL Lacs found with the photo- z technique.

Keywords: (galaxies:) BL Lacertae objects: general — galaxies: active

1. INTRODUCTION

Active galactic nuclei (AGNs) are laboratories for extreme physical processes that generate high luminosities (Urry & Padovani 1995). They are supermassive black holes at the center of galaxies (Fabian 2008), powered by active mass accretion (Marconi et al. 2004). The classification of AGN is based on their orientation relative to our line of sight (Urry & Padovani 1995). Blazars are a subclass of jetted AGN oriented with the relativistic jet pointing along the line of sight with a viewing angle $\theta_m < 1/\Gamma$, where Γ is the bulk Lorentz factor (Blandford & Rees 1978; Marcolilli et al. 2017). Blazars produce high-energy gamma-ray emission and show high variability (Perlman 2013). There are two characteristic bumps in the spectral energy distribution (SED) of blazars: the bump at lower energies (infrared to X-ray) is theorized to originate from synchrotron emission produced by electrons, and the bump at higher energies (X-ray to γ -ray) is interpreted as being due to inverse Compton scattering off either the synchrotron photons (Maraschi et al. 1994) or a circumnuclear photon field (Dermer & Schlickeiser 1994).

Blazars can be classified into different groups by their spectral properties (Padovani & Giommi 1995). Flat spectrum radio quasars (FSRQs) are blazars with broad emission lines in their spectra (equivalent width $> 5 \text{ \AA}$), while BL Lacs exhibit no or weak emission lines (equivalent width $\leq 5 \text{ \AA}$) (Maraschi et al. 1994; Ajello et al. 2013). The lack of prominent emission lines of BL Lacs makes it challenging to measure their redshifts. Indeed, around 40 % of BL Lacs in the Fourth LAT AGN Catalog Data Release 2 (4LAC-DR2) lack measured redshifts (Ajello et al. 2020; Lott et al. 2020b). Additionally, blazars can be classified according to the synchrotron peak frequency: low synchrotron peaked (LSP) blazars have a synchrotron bump at lower energies where $\nu_{\text{peak}}^S \leq 10^{14} \text{ Hz}$; intermediate synchrotron peaked (ISP) blazars have a synchrotron bump at intermediate

sheng2@clemson.edu

^a A member of the SARA Consortium

energies where $10^{14} \leq v_{\text{peak}}^S \leq 10^{15}$ Hz; high synchrotron peaked (HSP) blazars have a synchrotron bump at higher energies where $v_{\text{peak}}^S \geq 10^{15}$ Hz (Abdo et al. 2010).

Measuring redshifts of distant sources is essential in studying their energetic jets as well as a means of measuring the extragalactic background light (EBL, Ackermann et al. 2012). The EBL is the cumulative radiation from star formation and super-massive black hole accretion integrated over all redshifts. (Domínguez & Ajello 2015; Desai et al. 2019a). Direct measurements of the EBL are difficult because of the strong zodiacal light and foreground emission from our Galaxy (Moralejo et al. 2017). However, blazars can be utilized to measure the EBL as an alternative method to the direct measurement. The annihilation between γ -ray photons from blazars and EBL photons leaves a distinct attenuation in the spectra of blazars. This attenuation can be used to constrain the EBL models and its evolution with redshift (Biteau & Williams 2015; Abdollahi et al. 2018). Moreover, the attenuation increases as the redshift increases, motivating us to search for high-redshift sources.

Photometric redshift measurement has been applied to powerlaw sources like GRBs (Tagliaferri et al. 2005; Krühler et al. 2011). Rau et al. (2012) utilized the photometric method to measure the redshifts of blazars by fitting SED templates to multi-band photometry obtained by simultaneous *Swift*/UVOT (Roming et al. 2005) and Gamma-Ray burst Optical/NearInfrared Detector (GROND, Greiner et al. 2007) optical imaging. Photons from blazars are absorbed by the neutral hydrogen along the line of sight with a rest-wavelength blue-wards of 912Å (Lyman-limit) and 1216Å (Lyman- α forest), leaving two characteristic breaks in the source spectra. The breaks are redshift dependent and, therefore, can be used to measure the photometric redshift. The photometric technique enabled Rau et al. (2012) to measure the redshifts for nine BL Lacs out of a sample of 103 from the Second LAT AGN Catalog (2LAC) (Ackermann et al. 2011). Six of them were newly discovered BL Lacs with high redshifts ($z > 1.3$). Later, using the same technique except simultaneous observations, Kaur et al. (2017) found photometric redshifts for five sources from a sample of forty from the Third *Fermi* Large Area Telescope Source Catalog (3FGL) (Acero et al. 2015), and Kaur et al. (2018) discovered two more high- z BL Lacs. Rajagopal et al. (2020) continued the work and found three more sources with high redshifts, bringing the number of high- z BL Lacs found by this method up to 16.

Here we continue this campaign, using the Neil Gehrels *Swift* Observatory (Gehrels et al. 2004), 1.0 m SARA-RM (Southeastern Association for Research in Astronomy at Roque de los Muchachos, La Palma, Spain), and 0.6 m SARA-CT (Cerro Tololo, Chile) telescopes (Keel et al. 2016) to obtain magnitudes in 10 filters from ultraviolet to near infrared (nIR) ($uvw2$, $uvm2$, $uvw1$, u , b , v , g' , r' , i' , z') of the 60 selected sources. The photometric redshifts are estimated by the method developed by Rau et al. (2012), but the UVOT and SARA observations are not always simultaneous. A flat cosmological model Λ CDM with $H_0 = 73$ km/s/Mpc, $\Omega_m = 0.3$, $\Omega_\Lambda = 0.7$ is used in the content of this work. The structure of this paper is organized as follows: Section 2 introduces the instruments and observational methods used. Section 3 describes the procedures and techniques in the data analysis. Section 4 describes the SED fitting technique. Section 5 reports the redshifts for the sources we analyzed, which is followed by Section 6 that discusses our findings and applications of high- z BL Lacs. Section 7 is the summary of this work.

2. OBSERVATIONS

A sample of 60 BL Lacs with no redshift is selected from the 3FGL (Acero et al. 2015) and Third *Fermi*-LAT Catalog of High-Energy Sources (3FHL, Ajello et al. 2017). Of the 60 selected BL Lacs, 12 were observed during cycle 13¹, 16², and 17³ of the Neil Gehrels *Swift* Observatory Guest Investigator program. The rest were approved as Targets of Opportunity. The selected BL Lacs are observed in the UV-optical band with six filters ($uvw2$, $uvm2$, $uvw1$, u , b , v) on the UVOT instrument of *Swift*. The total exposure time of the UVOT instrument is ~ 2000 s for each source. The time assigned to each filter is weighted as $uvw2 : uvm2 : uvw1 : u : b : v = 4 : 3 : 2 : 1 : 1 : 1$

The selected targets are observed in the optical-nIR band from the ground using four SDSS filters (g' , r' , i' , z') installed on SARA-RM and SARA-CT. The exposure in every filter ranges from 15 to 40 minutes to ensure a good signal to noise ratio of the images. The time separation between the first and last filter is around 50 minutes to 1 hour and 30 minutes depending on the brightness of the sources. Table 1 shows the details of the observation of our sample.

3. DATA ANALYSIS AND CALIBRATIONS

3.1. SARA data analysis

We calibrate the images with bias, dark and flat frames using IRAF v2.61 (Image Reduction and Analysis Facility, Tody 1986): the bias frames remove the electronic background, the dark frames remove the current caused by thermal effect, and the flat frames

¹ Proposal: 1316180, PI: Dr. A. Kaur.

² Proposal: 1619148, PI: Dr. M. Rajagopal

³ Proposal: 1720112, PI: Dr. M. Rajagopal

correct pixel-to-pixel variations in the sensitivity of the CCD. The same IRAF software is also used to perform photometry. We use standard stars (Smith et al. 2006; Landolt 2009; Albareti et al. 2017) observed on the same night to calibrate the magnitudes of the sources. We measure the full width half maximum (FWHM) of the point-spread function for each night. A schematic representation of the source and background regions chosen for analysis are shown in Figure 1.

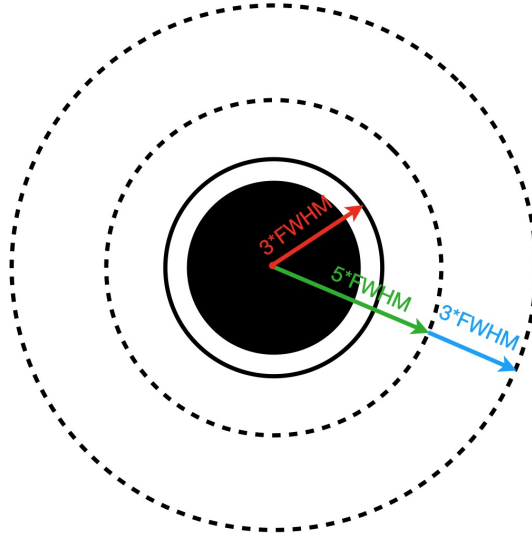


Figure 1. A circular region with radius of 3 times the FWHM is used as the source region. An annulus with inner radius of 5 times the FWHM and width of 3 times the FWHM is used as the background region. This setting makes the area of the background annulus ~ 4 times the area of the aperture, which ensures good statistics on the background estimation.

3.2. *Swift* UVOT data analysis

We analyze the UVOT data following the standard pipeline from Poole et al. (2008). The images are calibrated using the remote *Swift* Calibration Database (CALDB) v.1.0.2 to remove bad pixels, correct sensitivities, apply dark frames, etc. A circular region of $5''$ is used as the source region, and $20''$ to $30''$ is used as the background region. We use the command UVOTSOURCE provided in HEASoft v.6.28⁴ to extract the AB magnitudes from the images. If the image file contains multiple extensions, UVOTIMSUM is used to align and stack the extensions. Both SARA and *Swift* magnitudes are corrected for the Galactic foreground extinction (Kataoka et al. 2008).

3.3. Variability correction and cross-calibration

Blazars are highly variable in the optical band on timescales from minutes to days (Racine 1970; Carini et al. 1991; Urry 1993; Otero-Santos et al. 2022). Since both *Swift* and SARA telescopes observe the sources in sequence, we must account for the variability caused by the non-simultaneous observation as a part of the systematic uncertainty in our photo- z technique. Following Rau et al. (2012) and Rajagopal et al. (2020), we include a systematic uncertainty $\Delta = 0.1$ mag for both UVOT and SARA filters based on the changes in the observed magnitudes in the $uvw2$ filter.

Cross-calibration between UVOT and SARA filters is also performed following Rau et al. (2012). We assume that the SED of the sources of interest remains unchanged. We approximate the SED by a power law. Color terms $g' - r'$ and $b - g'$ are fitted using a quadratic equation (Rajagopal et al. 2020):

$$b - g' = 0.26(g' - r') + 0.02(g' - r')^2. \quad (1)$$

Using Equation 1, we calculate the offset in the b filter. This offset is applied to all UVOT filters. Cross-calibrated magnitudes are reported in Table 2.

4. SED FITTING

⁴ <https://heasarc.gsfc.nasa.gov/docs/software/heasoft/>

The FORTRAN code LePhare v.2.2 (Arnouts et al. 1999; Ilbert et al. 2006) is used to perform SED fitting and find the photometric redshifts. LePhare utilizes a χ^2 fitting technique to determine a best-fit SED model for each source, based on the observational data in 10 filters. Three different libraries are included during this fitting process. The first library contains 60 power-law ($F_\lambda \propto \lambda^{-\beta}$, $\beta \in [0, 3]$) templates. The second library consists of templates of normal galaxies and AGN/galaxy hybrids (Salvato et al. 2008, 2011), which are included to model host-galaxy-dominated sources. The third library is composed of various stellar templates to avoid false associations (Bohlin et al. 1995; Pickles 1998; Chabrier et al. 2000).

Table 1. *Swift*-UVOT and SARA Observations along with visual extinction values. $A_V = 3.1 \times E(B-V)$

3FGL or 3FHL (Name)	Counterpart (Name)	RA J2000 ^b (hh:mm:ss)	Dec J2000 ^b (° :′ :″)	Swift Date ^a (UT)	SARA Date ^a (UT)	A_V (mag)
3FGL J0009.3+5030	NVSS J000922+503028	00:09:22.76	+50:30:28.84	2018 Sep. 14	2021 Sep. 18	0.40
3FGL J0018.9–8152	PMN J0019–8152	00:19:20.64	−81:52:51.42	2019 Nov. 13	2021 Jul. 27	0.38
3FGL J0021.6–6835	PKS 0021–686	00:24:06.72	−68:20:54.59	2020 Oct. 21	2021 Jul. 29	0.07
3FGL J0244.4–8224	PMN J0251–8226	02:51:09.23	−82:26:29.24	2020 Oct. 22	2021 Jul. 29	0.26
3FHL J0301.4–5618	WISEA J030115.09–561643.5	03:01:14.72 ^c	−56:16:44.80 ^c	2021 Nov. 24	2021 Dec. 03	0.03
3FGL J0303.6+4716	4C +47.08	03:03:35.24	+47:16:16.28	2020 Jul. 21	2021 Sep. 18	0.68
3FHL J0319.2–7045	WISEA J032009.21–704533.6	03:20:07.32 ^c	−70:43:20.10 ^c	2021 Dec. 24	2021 Dec. 23	0.09
3FHL J0500.6+1903	...	05:00:42.98 ^c	+19:03:14.80 ^c	2021 Dec. 10	2022 Jan. 04	1.36
3FHL J0501.0+2425	1RXS J050107.1+242318	05:01:06.97 ^c	+24:23:16.32 ^c	2021 Dec. 31	2021 Dec. 23	1.37
3FGL J0706.5+3744	GB6 J0706+3744	07:06:31.70	+37:44:36.42	2015 May 18	2020 Oct. 28	0.19
3FGL J0707.0+7741	NVSS J070651+774137	07:06:51.33	+77:41:37.00	2020 Apr. 12	2021 Feb. 16	0.13
3FGL J0753.1+5353	4C +54.15	07:53:01.38	+53:52:59.63	2020 Aug. 18	2020 Oct. 28	0.11
3FGL J0754.4–1148	TXS 0752–116	07:54:26.46	−11:47:16.94	2020 Nov. 22	2021 Feb. 01	0.53
3FGL J0806.6+5933	SBS 0802+596	08:06:25.95	+59:31:06.92	2020 Jun. 10	2021 Feb. 01	0.16
3FGL J0816.7+5739	SBS 0812+578	08:16:22.73	+57:39:09.14	2022 May 31	2022 Apr. 09	0.14
3FGL J0839.6+1803	TXS 0836+182	08:39:30.72	+18:02:47.15	2021 Mar. 07	2022 Mar. 06	0.07
3FGL J0843.9+5311	NVSS J084411+531250	08:44:11.70	+53:12:50.58	2021 Mar. 30	2022 Mar. 11	0.07
3FGL J0849.3+0458	TXS 0846+051	08:49:32.55	+04:55:07.86	2021 Mar. 07	2021 Apr. 10	0.17
3FGL J0924.2+0534	RBS 0771	09:24:01.26	+05:33:42.70	2021 Oct. 15	2022 Jan. 04	0.12
3FGL J0942.1–0756	PMN J0942–0800	09:42:21.46	−07:59:53.20	2018 Dec. 19	2022 Feb. 13	0.08
3FGL J1027.7+6316	RX J1027.4+6317	10:27:25.12	+63:17:53.20	2020 Jul. 19	2021 Feb. 01	0.03
3FGL J1032.5+6623	SDSS J103239.06+662323.2	10:32:39.08	+66:23:23.21	2020 Apr. 03	2021 Feb. 16	0.04
3FGL J1101.5+4106	RX J1101.3+4108	11:01:24.73	+41:08:47.39	2021 Oct. 04	2022 Mar. 11	0.03
3FGL J1103.9–5357	PKS 1101–536	11:03:52.22	−53:57:00.68	2021 Oct. 16	2021 Dec. 23	0.76
3FHL J1127.8+3615	WISE J112758.88+362028.4	11:27:59.08 ^c	+36:20:33.09 ^c	2021 Jul. 18	2022 Mar. 11	0.06
3FGL J1224.6+4332	B3 1222+438	12:24:51.51	+43:35:19.28	2020 Nov. 15	2022 May 26	0.03
3FGL J1244.8+5707	1RXS J124510.5+571020	12:45:09.99	+57:09:54.36	2020 Nov. 30	2021 Feb. 16	0.03
3FGL J1249.7+3705	RX J1249.8+3708	12:49:46.75	+37:07:47.90	2021 May 06	2021 Jun. 12	0.04
3FGL J1256.7+5328	TXS 1254+538	12:56:38.630	+53:34:23.70	2020 Dec. 15	2021 Jun. 27	0.05
3FGL J1311.0+0036	RX J1311.1+0035	13:11:06.48	+00:35:10.03	2022 Apr. 13	2022 Feb. 26	0.08
3FGL J1327.9+2524	NVSS J132758+252750	13:27:58.93	+25:27:46.71	2021 Apr. 13	2022 Apr. 09	0.03
3FGL J1357.5+0125	RX J1357.6+0128	13:57:38.70	+01:28:13.62	2022 Apr. 26	2022 Apr. 21	0.09
3FGL J1419.5+0449	SDSS J141927.49+044513.7	14:19:27.74	+04:45:13.93	2022 Apr. 23	2022 Apr. 21	0.09

Table 1 continued on next page

Table 1 (*continued*)

3FGL or 3FHL (Name)	Counterpart (Name)	RA J2000 ^b (hh:mm:ss)	Dec J2000 ^b (° :′ :″)	Swift Date ^a (UT)	SARA Date ^a (UT)	Av (mag)
3FHL J1421.5–1654	WISEA J142128.94–165455.4	14:21:29.22 ^c	–16:54:55.13 ^c	2021 Aug. 29	2022 Feb. 13	0.24
3FGL J1424.3+0434	TXS 1421+048	14:24:09.50	+04:34:52.07	2022 Mar. 28	2022 Feb. 26	0.07
3FGL J1426.2+3402	RGB J1426+340	14:26:07.72	+34:04:26.33	2021 Apr. 10	2022 May 26	0.05
3FHL J1440.2–2343	WISEA J143959.46–234141.0	14:39:59.46 ^c	–23:41:41.0 ^c	2021 Sep. 15	2021 Aug. 20	0.30
3FGL J1446.1–1628	PKS B1443–162	14:45:53.38	–16:29:01.61	2022 Jan. 03	2022 Feb. 26	0.29
3FGL J1454.5+5124	TXS 1452+516	14:54:27.12	+51:24:33.73	2021 Jul. 01	2022 May 06	0.04
3FGL J1509.7+5556	SBS 1508+561	15:09:47.95	+55:56:17.30	2021 May 17	2021 Jul. 02	0.04
3FGL J1531.0+5737	87GB 152947.5+574636	15:30:58.34	+57:36:25.06	2021 May 22	2022 May 06	0.04
3FGL J1533.5+3416	RX J1533.3+3416	15:33:24.26	+34:16:40.22	2021 May 24	2021 Aug. 07	0.06
3FGL J1534.4+5323	1ES 1533+535	15:35:00.81	+53:20:37.21	2021 May 31	2022 May 06	0.05
3FGL J1550.3+7409	87GB 155014.9+741816	15:49:27.28	+74:09:32.18	2020 Sep. 29	2021 Jun. 12	0.07
3FGL J1549.0+6309	SDSS J154958.45+631021.2	15:49:57.32	+63:10:7.32	2021 Jan. 07	2021 Jun. 12	0.05
3FGL J1630.7+5222	TXS 1629+524	16:30:43.15	+52:21:38.63	2021 Jul. 10	2021 Jul. 02	0.07
3FGL J1637.1+1314	1RXS J163717.1+131418	16:37:16.74	+13:14:38.80	2021 Jul. 17	2022 May 06	0.16
3FGL J1651.6+7219	RX J1651.6+7218	16:51:39.95	+72:18:25.13	2022 Apr. 17	2022 May 26	0.11
3FGL J1829.8+1328	MG1 J183001+1323	18:30:00.76	+13:24:14.33	2021 Nov. 11	2022 May 06	0.67
3FGL J1848.9+4247	RGB J1848+427	18:48:47.17	+42:45:34.92	2021 Nov. 17	2022 May 06	0.22
3FGL J1927.7+6118	S4 1926+61	19:27:30.44	+61:17:32.87	2021 Sep. 06	2021 Sep. 18	0.17
3FGL J2007.7–7728	PKS 2000–776	20:12:30.18	–16:46:50.48	2020 Jul. 20	2021 Jun. 11	0.32
3FGL J2012.1–1643	PMN J2012–1646	20:12:30.18	–16:46:50.48	2020 Jul. 18	2020 Oct. 28	0.32
3FGL J2107.7–4822	PMN J2107–4827	21:07:44.48	–48:28:03.00	2017 Sep. 08	2021 Jul. 27	0.10
3FGL J2139.4–4235	MH 2136–428	21:39:24.17	–42:35:20.00	2020 Sep. 25	2021 Jul. 27	0.05
3FGL J2149.6+1915	TXS 2147+191	21:49:47.31	+19:20:46.07	2020 Aug. 25	2021 Jul. 02	0.31
3FGL J2159.8+1025	TXS 2157+102	22:00:07.93	+10:30:07.88	2020 Oct. 21	2020 Oct. 28	0.17
3FGL J2236.0–3629	NVSS J223554–362901	22:35:54.83	–36:29:02.87	2020 Oct. 30	2021 Jul. 29	0.04
3FGL J2236.2–5049	SUMSS J223605–505521	22:36:05.64	–50:55:19.92	2020 Aug. 04	2021 Jul. 29	0.04
3FGL J2240.9+4121	B3 2238+410	22:41:07.20	+41:20:11.62	2021 Aug. 01	2021 Aug. 07	0.65

^a The beginning date of the exposures for Swift and SARA.^b The coordinates are from the 3FGL catalog, which are submitted to *Swift* for the UVOT observation and SARA telescopes for the optical observation.^c The coordinates are determined by the method discussed in Joffre et al. (2022); Stroh & Falcone (2013); Paiano et al. (2017); Silver et al. (2020); Kerby et al. (2021)

Table 2. *Swift*-UVOT and SARA photometry (AB magnitudes corrected for extinction)

3FGL or 3FHBL Name	g'	r'	i'	z'	$uvw2$	$uvw1$	u	b	v
3FGL J0009.3+5030	18.38±0.01	18.06±0.01	17.78±0.01	17.50±0.02	20.25±0.16	20.15±0.19	19.55±0.15	19.10±0.13	18.46±0.12
3FGL J0018.9-8152	17.60±0.02	17.16±0.01	16.84±0.01	16.67±0.03	18.87±0.07	18.91±0.09	18.51±0.08	18.08±0.06	17.72±0.06
3FGL J0021.6-6835	18.02±0.01	17.58±0.01	17.52±0.01	16.84±0.03	20.03±0.07	19.72±0.08	19.35±0.07	18.60±0.05	18.14±0.05
3FGL J0244.4-8224	18.70±0.02	18.49±0.02	18.30±0.03	17.89±0.06	19.54±0.09	19.60±0.13	19.87±0.16	19.16±0.13	18.75±0.15
3FHL J0301.4-5618	19.08±0.02	18.56±0.01	18.27±0.02	17.53±0.04	>21.91	>21.42	20.44±0.23	19.46±0.18	19.22±0.26
3FGL J0303.6+4716	16.59±0.00	16.13±0.00	15.86±0.00	15.57±0.00	18.61±0.22	18.51±0.24	17.91±0.17	17.13±0.11	16.71±0.12
3FHL J0319.2-7045	19.72±0.07	18.96±0.03	18.59±0.04	17.60±0.05	21.00±0.17	20.74±0.22	20.71±0.29	20.52±0.36	19.92
3FHL J0500.6+1903	19.73±0.09	19.18±0.05	19.35±0.07	19.45±0.21	>18.05	>20.44	>20.27	>20.28	>19.88
3FHL J0501.0+2425	18.50±0.08	18.05±0.04	17.89±0.05	18.26±0.16	>19.11	>19.24	>19.01	18.86±0.32	>18.62
3FGL J0706.5+3744	18.01±0.01	17.59±0.01	17.24±0.01	17.30±0.02	19.07±0.07	19.05±0.09	18.82±0.07	18.42±0.09	18.13±0.11
3FGL J0707.0+7741	17.63±0.00	17.08±0.00	16.83±0.00	16.50±0.01	18.88±0.08	19.06±0.11	18.68±0.10	18.01±0.08	17.78±0.10
3FGL J0753.1+5353	19.87±0.04	19.42±0.03	19.31±0.05	18.83±0.09	22.06±0.30	>22.07	21.42±0.32	>20.73	>19.99
3FGL J0754.4-1148	19.98±0.04	19.05±0.02	18.75±0.03	18.52±0.08	22.69±0.35	>22.47	22.09±0.32	21.33±0.24	20.25±0.16
3FGL J0806.6+5933	18.93±0.01	18.43±0.01	17.77±0.01	17.58±0.03	20.33±0.09	20.09±0.10	20.05±0.11	19.48±0.11	19.06±0.13
3FGL J0816.7+5739	17.03±0.01	16.62±0.00	16.34±0.01	16.18±0.01	18.24±0.07	18.13±0.09	17.84±0.09	17.19±0.08	17.13±0.11
3FGL J0839.6+1803	17.81±0.01	17.33±0.01	17.02±0.01	16.56±0.02	17.84±0.14	18.74±0.09	18.49±0.09	18.19±0.10	17.94±0.14
3FGL J0843.9+5311	17.71±0.00	17.42±0.00	17.17±0.01	17.05±0.01	19.25±0.10	19.23±0.13	18.86±0.12	18.36±0.12	17.79±0.13
3FGL J0849.3+0458	18.90±0.03	18.61±0.03	18.18±0.03	18.07±0.10	>18.75	19.58±0.19	19.05±0.15	18.97±0.21	>18.98
3FGL J0924.2+0534	18.20±0.01	17.85±0.01	17.65±0.01	17.48±0.03	18.85±0.07	18.62±0.09	18.81±0.09	18.46±0.11	18.29±0.17
3FGL J0942.1-0756	19.30±0.08	19.04±0.06	18.83±0.07	17.90±0.06	21.02±0.13	20.79±0.17	20.82±0.17	20.07±0.15	19.37±0.14
3FGL J1027.7+6316	19.31±0.03	19.17±0.03	18.99±0.04	18.81±0.09	20.42±0.10	20.24±0.12	20.08±0.16	19.52±0.17	19.34±0.24
3FGL J1032.5+6623	19.73±0.01	19.27±0.01	19.09±0.01	19.03±0.06	>22.11	>21.73	20.34±0.19	20.01±0.22	19.86±0.36
3FGL J1101.5+4106	18.43±0.01	18.28±0.01	18.11±0.01	18.07±0.03	19.23±0.09	19.00±0.11	18.91±0.11	18.77±0.18	>18.01
3FGL J1103.9-5357	15.68±0.01	15.08±0.01	14.63±0.01	14.50±0.01	16.83±0.10	17.55±0.19	16.11±0.09	15.89±0.07	15.38±0.10
3FHL J1127.8+3615	20.48±0.03	20.34±0.03	20.35±0.04	20.22±0.11	21.73±0.13	21.48±0.14	21.30±0.17	20.79±0.24	>20.51
3FGL J1224.6+4332	25.31±0.02	25.18±0.02	25.86±0.03	27.45±0.07	>27.61	>27.12	>26.82	>26.15	>25.34
3FGL J1244.8+5707	18.91±0.01	18.55±0.01	18.31±0.01	17.90±0.03	20.11±0.07	19.95±0.08	19.75±0.08	19.33±0.07	19.01±0.08
3FGL J1249.7+3705	19.25±0.01	18.98±0.01	18.88±0.01	18.75±0.05	19.93±0.28	>24.44	>24.09	>23.72	>22.81
3FGL J1256.7+5328	21.84±0.08	20.90±0.05	20.46±0.09	19.93±0.28	>24.44	>24.09	>23.72	>22.81	>21.10
3FGL J1311.0+0036	18.81±0.03	18.20±0.02	17.71±0.02	17.45±0.05	20.16±0.09	20.02±0.11	20.01±0.12	19.35±0.11	18.98±0.14
3FGL J1327.9+2524	21.40±0.08	20.85±0.07	21.26±0.22	...	>23.86	>23.41	>22.99	>22.32	>21.54
3FGL J1357.5+0125	18.08±0.01	17.99±0.01	17.55±0.01	16.87±0.03	18.90±0.08	18.64±0.10	18.09±0.09	18.11±0.14	17.52±0.17
3FGL J1419.5+0449	18.54±0.02	18.52±0.01	18.44±0.02	17.98±0.05	>21.68	>21.19	19.70±0.16	18.69±0.13	18.55±0.19

Table 2 continued on next page

Table 2 (*continued*)

3FHL or 3FHBL Name	g'	r'	i'	z'	$uvw2$	$uvw1$	u	b	v
3FHL J1421.5-1654	19.30±0.04	18.94±0.03	18.75±0.04	17.95±0.06	21.04±0.26	20.20±0.20	20.67±0.21	20.03±0.32	>19.39
3FGL J1424.3+0434	18.38±0.02	17.96±0.02	17.59±0.02	17.19±0.04	19.97±0.09	19.89±0.14	19.54±0.11	18.95±0.13	18.34±0.22
3FGL J1426.2+3402	22.26±0.01	22.44±0.01	23.35±0.01	25.47±0.02	23.44±0.08	23.23±0.09	23.24±0.10	22.53±0.09	22.22±0.10
3FHL J1440.2-2343	19.01±0.04	18.40±0.02	17.78±0.04	20.26±0.16	20.15±0.19	20.19±0.26	>19.93	>19.18	>18.41
3FGL J1446.1-1628	20.60±0.14	20.04±0.07	19.72±0.09	...	>22.76	>22.36	>22.04	>21.50	>20.75
3FGL J1454.5+5124	16.13±0.00	15.74±0.00	15.45±0.00	15.26±0.00	17.17±0.05	17.05±0.06	16.77±0.06	16.46±0.05	16.02±0.08
3FGL J1509.7+5556	17.87±0.00	17.54±0.00	17.30±0.01	17.14±0.03	19.00±0.07	18.92±0.09	18.80±0.09	18.38±0.08	17.96±0.08
3FGL J1531.0+5737	19.68±0.01	19.25±0.01	18.96±0.02	18.79±0.06	21.77±0.16	21.15±0.16	21.12±0.17	20.24±0.14	19.80±0.16
3FGL J1533.5+3416	18.10±0.01	17.86±0.01	17.70±0.01	17.77±0.03	19.08±0.08	19.06±0.09	18.83±0.09	18.29±0.08	18.17±0.11
3FGL J1534.4+5323	18.26±0.01	18.00±0.01	17.79±0.01	17.68±0.02	18.94±0.06	18.73±0.07	18.66±0.07	18.47±0.07	18.33±0.09
3FGL J1550.3+7409	19.88±0.01	19.29±0.01	19.06±0.01	18.73±0.04	21.58±0.18	22.28±0.33	21.29±0.25	20.64±0.32	>20.05
3FGL J1549.0+6309	20.40±0.02	19.74±0.01	19.22±0.02	19.24±0.08	22.11±0.25	>22.06	21.61±0.28	>21.33	>20.59
3FGL J1630.7+5222	16.77±0.00	16.51±0.00	16.27±0.00	16.08±0.01	17.96±0.07	17.85±0.08	17.48±0.07	17.26±0.07	16.84±0.08
3FGL J1637.1+1314	19.75±0.01	19.42±0.01	19.09±0.02	18.65±0.06	21.00±0.12	20.69±0.14	20.64±0.16	20.05±0.16	19.84±0.22
3FGL J1651.6+7219	23.45±0.01	23.53±0.01	24.31±0.01	26.38±0.04	24.46±0.10	24.25±0.12	24.38±0.15	23.81±0.14	23.43±0.17
3FGL J1829.8+1328	18.06±0.01	17.52±0.01	17.11±0.01	17.15±0.01	>20.23	>19.93	19.30±0.26	19.28±0.35	18.20±0.23
3FGL J1848.9+4247	19.16±0.01	18.87±0.01	18.61±0.02	18.35±0.05	19.88±0.11	19.80±0.15	19.74±0.18	19.40±0.26	>19.24
3FGL J1927.7+6118	18.09±0.01	17.58±0.01	17.25±0.01	16.92±0.09	19.62±0.10	19.43±0.10	19.18±0.09	18.61±0.08	18.23±0.08
3FGL J2007.7-7728	20.26±0.06	19.70±0.04	19.61±0.08	19.26±0.19	>22.01	>21.73	>21.48	>21.08	>20.41
3FGL J2012.1-1643	20.01±0.06	19.98±0.07	19.72±0.06	20.13±0.26	>22.27	>22.03	>21.48	>20.79	>20.02
3FGL J2107.7-4822	20.09±0.07	19.29±0.03	18.71±0.03	18.38±0.08	21.87±0.22	21.78±0.27	>21.73	>21.06	>20.30
3FGL J2139.4-4235	16.40±0.01	15.86±0.00	15.57±0.00	15.31±0.01	17.76±0.04	17.61±0.05	17.38±0.05	16.98±0.04	16.55±0.04
3FGL J2149.6+1915	20.63±0.04	20.33±0.04	20.39±0.09	21.06±0.57	21.33±0.15	21.88±0.29	21.48±0.26	20.70±0.20	>20.71
3FGL J2159.8+1025	19.17±0.03	18.68±0.02	18.29±0.02	18.13±0.04	>21.44	20.36±0.30	20.63±0.35	>20.06	>19.30
3FGL J2236.0-3629	19.00±0.02	18.42±0.01	18.32±0.02	18.20±0.06	19.11±0.07	21.38±0.15	21.16±0.12	20.10±0.09	19.16±0.07
3FGL J2236.2-5049	18.65±0.02	18.39±0.01	18.32±0.02	17.98±0.05	>20.98	>20.40	20.16±0.35	>19.49	>18.72
3FGL J2240.9+4121	17.92±0.01	17.54±0.01	17.29±0.01	17.14±0.02	19.43±0.22	>19.73	18.76±0.18	18.44±0.16	18.03±0.17

Table 3. SED fitting

3FGL or 3FHL Name	$z_{\text{phot,best}}^a$	Power Law Template				Galaxy Template			
		z_{phot}^b	χ^2	P_z^d	β^e	z_{phot}^b	χ^2	P_z^d	Model
Sources with confirmed photometric redshifts									
3FHL J0301.4–5618	$1.74^{+0.05}_{-0.08}$	$1.74^{+0.05}_{-0.08}$	8.1	95.5	1.90	$1.33^{+0.06}_{-0.05}$	7.9	99.4	
3FGL J1032.5+6623	$1.88^{+0.07}_{-0.03}$	$1.88^{+0.07}_{-0.03}$	8.7	98.5	1.00	$1.49^{+0.39}_{-0.01}$	13.6	36.5	I22491_40_TQSO1_60.sed
3FGL J1419.5+0449	$2.10^{+0.03}_{-0.04}$	$2.10^{+0.03}_{-0.04}$	22.4	100.0	0.95	$1.73^{+0.01}_{-0.04}$	3.6	96.8	CB1_0_LOIII4.sed
Sources with photometric redshift upper limits									
3FGL J0009.3+5030	< 1.65	$1.53^{+0.12}_{-0.19}$	10.2	63.9	1.40	$0.00^{+0.02}_{-0.00}$	10.5	88.3	Spi4_template_norm.sed
3FGL J0018.9–8152	< 1.03	$0.79^{+0.24}_{-0.79}$	4.2	32.2	1.40	$0.00^{+0.01}_{-0.00}$	6.4	98.2	I22491_80_TQSO1_20.sed
3FGL J0021.6–6835	< 1.50	$1.42^{+0.08}_{-0.18}$	13.6	72.8	1.55	$0.00^{+0.01}_{-0.00}$	34.3	99.1	Spi4_template_norm.sed
3FGL J0244.4–8224	< 0.92	$0.06^{+0.86}_{-0.06}$	11.3	17.7	1.10	$0.04^{+0.02}_{-0.03}$	8.9	69.6	I22491_60_TQSO1_40.sed
3FGL J0303.6+4716	< 1.47	$1.36^{+0.11}_{-0.08}$	7.3	65.5	1.60	$0.00^{+0.04}_{-0.00}$	10.5	96.5	Mrk231_template_norm.sed
3FHL J0319.2–7045	...	$3.06^{+0.02}_{-0.00}$	82.0	99.3	1.70	$0.64^{+0.13}_{-0.05}$	22.7	65.7	Mrk231_template_norm.sed
3FHL J0500.6+1903 ^f	$2.97^{+0.04}_{-2.97}$	1.6	78.9	pl_QSO_DR2_029_t0.spec
3FHL J0501.0+2425	...	$2.82^{+0.13}_{-0.31}$	9.3	41.3	0.60	$2.84^{+0.15}_{-2.84}$	8.8	87.0	pl_QSO_DR2_029_t0.spec
3FGL J0706.5+3744	< 1.04	$0.03^{+1.01}_{-0.03}$	6.3	13.7	1.20	$0.00^{+0.02}_{-0.00}$	6.7	81.1	I22491_60_TQSO1_40.sed
3FGL J0707.0+7741	< 0.96	$0.09^{+0.87}_{-0.09}$	7.6	19.0	1.55	$0.00^{+0.02}_{-0.00}$	11.6	91.3	I22491_90_TQSO1_10.sed
3FGL J0753.1+5353	< 1.69	$1.63^{+0.06}_{-0.10}$	11.2	72.7	1.90	$0.00^{+0.05}_{-0.00}$	7.2	91.4	M82_template_norm.sed
3FGL J0754.4–1148	< 2.82	$2.73^{+0.09}_{-0.20}$	23.0	66.0	2.00	$0.01^{+0.05}_{-0.01}$	5.8	93.8	Sey2_template_norm.sed
3FGL J0806.6+5933	< 0.94	$0.12^{+0.82}_{-0.12}$	10.8	23.4	1.75	$0.10^{+0.03}_{-0.03}$	15.1	93.4	Sey18_template_norm.sed
3FGL J0816.7+5739	< 1.22	$0.99^{+0.23}_{-0.99}$	3.7	34.3	1.25	$0.00^{+0.04}_{-0.00}$	10.3	92.7	I22491_70_TQSO1_30.sed
3FGL J0839.6+1803	< 0.93	$0.24^{+0.69}_{-0.24}$	22.9	26.0	1.35	$0.13^{+0.09}_{-0.04}$	16.6	82.5	I22491_70_TQSO1_30.sed
3FGL J0843.9+5311	< 1.44	$1.08^{+0.36}_{-1.08}$	8.6	32.6	1.35	$0.00^{+0.01}_{-0.00}$	8.2	97.9	I22491_80_TQSO1_20.sed
3FGL J0849.3+0458	< 1.14	$0.12^{+1.02}_{-0.12}$	15.1	19.0	1.30	$0.13^{+0.04}_{-0.02}$	5.4	37.5	I22491_40_TQSO1_60.sed
3FGL J0924.2+0534	< 0.94	$0.24^{+0.70}_{-0.24}$	4.2	25.7	0.85	$0.23^{+0.02}_{-0.08}$	2.6	64.5	I22491_40_TQSO1_60.sed
3FGL J0942.1–0756	< 1.10	$0.06^{+1.04}_{-0.06}$	17.6	14.6	1.75	$0.00^{+0.02}_{-0.00}$	16.8	97.0	I22491_template_norm.sed.save
3FGL J1027.7+6316	< 1.19	$1.06^{+0.13}_{-1.06}$	2.8	34.3	0.85	$1.43^{+0.02}_{-0.10}$	5.6	87.1	pl_I22491_30_TQSO1_70.sed
3FGL J1101.5+4106	< 1.26	$1.13^{+0.13}_{-1.13}$	0.8	36.1	0.60	$0.02^{+0.02}_{-0.02}$	3.6	14.1	pl_I22491_10_TQSO1_90.sed
3FGL J1103.9–5357	...	$0.81^{+0.15}_{-0.81}$	36.8	35.1	1.70	$0.00^{+0.06}_{-0.00}$	45.7	91.9	I22491_template_norm.sed.save
3FHL J1127.8+3615	< 1.65	$1.52^{+0.13}_{-0.22}$	3.9	67.9	0.55	$1.09^{+0.35}_{-0.10}$	4.7	66.0	pl_QSOH_template_norm.sed
3FGL J1224.6+4332	...	$2.37^{+0.08}_{-0.02}$	158.0	94.5	3.00	$0.61^{+2.44}_{-0.01}$	198.0	21.7	pl_QSOH_template_norm.sed
3FGL J1244.8+5707	< 1.06	$0.06^{+1.00}_{-0.06}$	1.9	15.3	1.30	$0.00^{+0.02}_{-0.00}$	5.2	95.9	I22491_70_TQSO1_30.sed
3FGL J1249.7+3705	< 1.25	$1.06^{+0.19}_{-1.06}$	0.7	33.1	0.75	$0.00^{+0.02}_{-0.00}$	2.2	27.5	pl_I22491_20_TQSO1_80.sed
3FGL J1256.7+5328	< 3.39	$3.20^{+0.19}_{-0.14}$	0.2	86.0	2.00	$0.40^{+0.05}_{-0.38}$	0.1	44.6	S0_90_QSO2_10.sed
3FGL J1311.0+0036	...	$0.93^{+0.01}_{-0.02}$	217.0	65.9	0.35	$0.29^{+0.02}_{-0.01}$	181.0	99.6	pl_TQSO1_template_norm.sed
3FGL J1327.9+2524	< 3.66	$3.54^{+0.12}_{-0.17}$	0.7	86.7	3.00	$2.60^{+0.11}_{-0.13}$	0.2	78.9	Mrk231_template_norm.sed
3FGL J1357.5+0125	< 1.09	$0.12^{+0.97}_{-0.12}$	28.2	20.3	0.95	$0.85^{+0.05}_{-0.04}$	21.8	90.9	I22491_80_TQSO1_20.sed
3FHL J1421.5–1654	< 1.30	$0.60^{+0.70}_{-0.60}$	13.9	24.1	1.65	$0.00^{+0.05}_{-0.00}$	15.1	74.2	I22491_template_norm.sed.save
3FGL J1424.3+0434	< 1.10	$0.06^{+1.04}_{-0.06}$	2.1	14.7	1.70	$0.00^{+0.01}_{-0.00}$	8.5	95.9	I22491_template_norm.sed.save

Table 3 continued on next page

Table 3 (continued)

3FGL or 3FHL Name	$z_{\text{phot,best}}^a$	Power Law Template				Galaxy Template				Model
		z_{phot}^b	$\chi^2 c$	P_z^d	β^e	z_{phot}^b	$\chi^2 c$	P_z^d		
3FGL J1426.2+3402	...	$0.57^{+0.48}_{-0.55}$	370.0	29.8	3.00	$0.59^{+0.03}_{-0.03}$	557.0	99.9	pl_QSOH_template_norm.sed	
3FHL J1440.2–2343	...	$2.36^{+0.20}_{-0.00}$	63.3	71.8	1.95	$0.29^{+0.05}_{-0.01}$	3.5	77.8	Mrk231_template_norm.sed	
3FGL J1446.1–1628 ^f	
3FGL J1454.5+5124	< 1.06	$0.12^{+0.94}_{-0.12}$	1.9	20.7	1.15	$0.00^{+0.03}_{-0.00}$	4.9	89.3	I22491_60.TQSO1_40.sed	
3FGL J1509.7+5556	< 1.04	$0.03^{+1.01}_{-0.03}$	1.9	13.7	1.20	$0.00^{+0.03}_{-0.00}$	2.1	90.6	I22491_60.TQSO1_40.sed	
3FGL J1531.0+5737	...	$1.25^{+0.22}_{-1.23}$	351.0	34.8	0.30	$0.91^{+0.09}_{-0.29}$	237.0	76.4	CB1_0_LOIII4.sed	
3FGL J1533.5+3416	< 1.45	$1.16^{+0.29}_{-0.32}$	9.7	40.3	0.80	$1.14^{+0.21}_{-0.05}$	10.8	76.6	pl_QSOH_template_norm.sed	
3FGL J1534.4+5323	< 1.11	$0.56^{+0.55}_{-0.56}$	1.8	27.6	0.75	$0.02^{+0.02}_{-0.02}$	1.9	24.5	pl_I22491_10.TQSO1_90.sed	
3FGL J1550.3+7409	< 1.65	$1.63^{+0.02}_{-1.63}$	11.9	25.2	1.75	$0.07^{+0.01}_{-0.01}$	5.1	99.9	Mrk231_template_norm.sed	
3FGL J1549.0+6309	< 2.94	$2.53^{+0.41}_{-0.11}$	29.9	52.9	1.85	$0.16^{+0.04}_{-0.05}$	9.2	99.5	M82_template_norm.sed	
3FGL J1630.7+5222	< 1.22	$1.04^{+0.18}_{-1.04}$	3.1	34.2	1.10	$0.00^{+0.04}_{-0.00}$	7.1	98.0	I22491_60.TQSO1_40.sed	
3FGL J1637.1+1314	...	$0.26^{+0.78}_{-0.26}$	238.0	23.6	0.60	$1.00^{+0.02}_{-0.04}$	133.0	65.5	CB1_0_LOIII4.sed	
3FGL J1651.6+7219	...	$1.04^{+0.13}_{-0.26}$	291.0	40.7	3.00	$0.59^{+0.03}_{-0.03}$	436.0	99.9	pl_QSOH_template_norm.sed	
3FGL J1829.8+1328	
3FGL J1848.9+4247	...	$0.26^{+0.61}_{-0.26}$	134.0	27.9	0.70	$0.54^{+0.03}_{-0.03}$	77.1	99.7	I22491_template_norm.sed.save	
3FGL J1927.7+6118	< 1.10	$0.10^{+1.00}_{-0.10}$	1.7	18.8	1.65	$0.00^{+0.01}_{-0.00}$	12.9	92.5	I22491_template_norm.sed.save	
3FGL J2007.7–7728	< 3.36	$3.07^{+0.29}_{-0.55}$	0.6	64.6	0.85	$3.10^{+0.06}_{-3.10}$	0.9	55.1	pl_QSOH_template_norm.sed	
3FGL J2012.1–1643	< 3.14	$2.76^{+0.38}_{-0.11}$	3.2	80.5	0.00	$2.67^{+0.29}_{-0.02}$	2.3	84.2	CB1_0_LOIII4.sed	
3FGL J2107.7–4822	...	$2.98^{+0.27}_{-0.02}$	33.9	90.0	1.95	$0.16^{+0.05}_{-0.06}$	11.7	92.0	Sey2_template_norm.sed	
3FGL J2139.4–4235	< 0.96	$0.03^{+0.93}_{-0.03}$	2.2	14.7	1.55	$0.00^{+0.02}_{-0.00}$	8.8	97.3	I22491_90.TQSO1_10.sed	
3FGL J2149.6+1915	< 1.15	$0.82^{+0.33}_{-0.82}$	15.8	28.2	0.80	$1.12^{+0.08}_{-0.09}$	11.3	92.3	pl_QSOH_template_norm.sed	
3FGL J2159.8+1025	< 2.64	$1.90^{+0.74}_{-0.00}$	16.4	33.3	2.00	$0.05^{+0.06}_{-0.05}$	9.2	95.6	M82_template_norm.sed	
3FGL J2236.0–3629	...	$1.93^{+0.12}_{-0.10}$	96.5	93.4	1.70	$0.03^{+0.03}_{-0.03}$	69.5	100.0	Mrk231_template_norm.sed	
3FGL J2236.2–5049	< 2.76	$2.62^{+0.14}_{-0.09}$	7.5	72.9	0.85	$2.57^{+0.08}_{-0.01}$	6.3	79.5	pl_QSOH_template_norm.sed	
3FGL J2240.9+4121	< 1.68	$1.53^{+0.15}_{-0.19}$	5.2	49.1	1.20	$0.00^{+0.02}_{-0.00}$	8.1	92.2	I22491_80.TQSO1_20.sed	

^a Best-fit or upper limit of the photometric redshift.^b Photometric redshifts with 1 σ confidence level.^c χ^2 value for ten degrees of freedom.^d Redshift probability density at $z_{\text{phot}} \pm 0.1(1+z_{\text{phot}})$.^e Spectral slope for the power-law model of the form $F_\lambda \propto \lambda^{-\beta}$.^f The fittings are not reported because they are not good ($\chi^2 = 0$) due to upper limits for six or more filters.

Following the criteria simulated in [Rajagopal et al. \(2020\)](#), sources with $z > 1.3$ and $E(B-V) \leq 0.30$ have reliable measured photometric redshifts within $|\Delta z/(1+z_{\text{sim}})| < 0.15$ accuracy, where z_{sim} is the input redshift for the simulation. Another criterion is the integral of probability density function $P_z > 90\%$, which indicates that the measured redshift is within $0.1(1+z_{\text{phot}})$ of the best-fit value. Reliable upper limits from the power-law model are provided for sources with $P_z \leq 90\%$ and $\chi^2 \leq 30$ for ten degrees of freedom. Specifically, we only report the photometric magnitudes for sources with $E(B-V) > 0.3$.

5. RESULTS

The best-fit photometric redshifts or upper limits for the BL Lacs, along with the χ^2 and P_z values for the power-law and galaxy template models are reported in Table 3. Three high- z BL Lacs are found from the analysis of sixty BL Lacs, while forty-one are reported with reliable upper limits. The SEDs in UVOT and SARA filters for the four high- z sources are presented in Figure 2. Under the criteria mentioned above ($P_z \geq 90\%$, $E(B-V) \leq 0.3$, and $z > 1.3$), the three high- z sources are 3FHL J0301.4–5618, 3FGL J1032.5+6623, and 3FGL J1419.5+0449. The redshifts of the three sources are $1.74^{+0.05}_{-0.08}$, $1.88^{+0.07}_{-0.03}$, and

$2.10^{+0.03}_{-0.04}$ for power-law templates, respectively. We also obtained redshifts using galaxy templates at $1.33^{+0.06}_{-0.05}$, $1.49^{+0.39}_{-0.01}$, and $1.73^{+0.01}_{-0.04}$. However, 3FGL J1032.5+6623 and 3FGL J1419.5+0449 have been identified as BL Lacs in the Fourth Fermi Large Area Telescope Source Catalog (4FGL, Abdollahi et al. 2020), and therefore the redshifts determined by the galaxy templates are not likely. Although 3FHL J0301.4–5618 is unclassified in the 3FGL and 4FGL catalog, it lies in the BL Lac group in the blazar sequence and *Fermi* blazar divide plots (see section 6). Therefore, the redshift determined by the power-law templates is more likely.

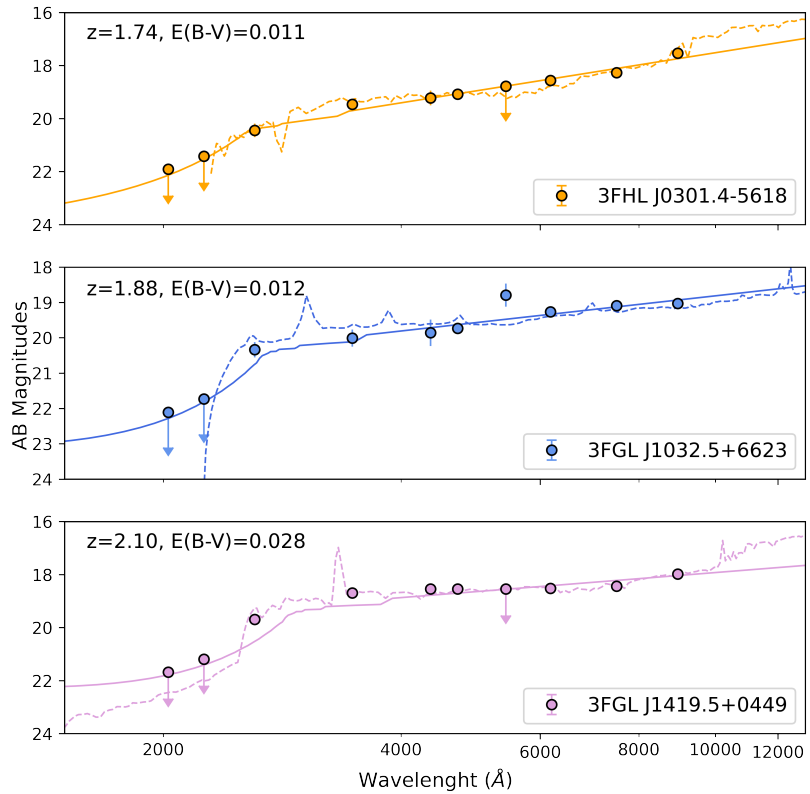


Figure 2. The SEDs of the three high-redshift BL Lacs. The solid circles with black edges represent photometric magnitudes from *Swift*-UVOT, SARA-CT, and SARA-RM. The magnitudes are ordered in the following way: *uw2*, *um2*, *uw1*, *uuu*, *ubb*, *g'*, *uvv*, *r'*, *i'*, *z'*. The solid and dashed lines are power-law and galaxy models, respectively.

6. DISCUSSIONS

6.1. Cosmic Gamma-ray Horizon

Very high energy (VHE) photons (>100 GeV) do not travel unimpeded. The extragalactic background light (EBL) impedes the travel of VHE photons via photon-photon interactions in the ultraviolet, optical, and infrared bands. Due to these interactions there is a redshift dependent opacity for high-energy photons in the universe (Finke et al. 2010; Domínguez & Ajello 2015). This opacity to VHE photons is evaluated by the cosmic gamma-ray horizon (CGRH, Domínguez et al. 2013). The CGRH is defined as the energy at which the optical depth is one ($\tau = 1$), and it is a function of redshift.

Figure 3 shows the highest photon energy versus redshift for different CGRH models. As is made apparent by this figure, there were not many BL Lacs probing the CGRH at high- z before our campaigns. As can be seen, our photometric method is efficient at finding these missing high- z sources. In this work, we find four high- z sources: 3FGL J1419.5+0449 ($\tau = 0.16^{+0.05}_{-0.03}$, $E_{\max} = 29$ GeV), 3FGL J1032.5+6623 ($\tau = 0.44^{+0.12}_{-0.08}$, $E_{\max} = 49$ GeV), 3FHL J0301.4–5618 ($\tau = 0.05^{+0.02}_{-0.01}$, $E_{\max} = 22$ GeV).

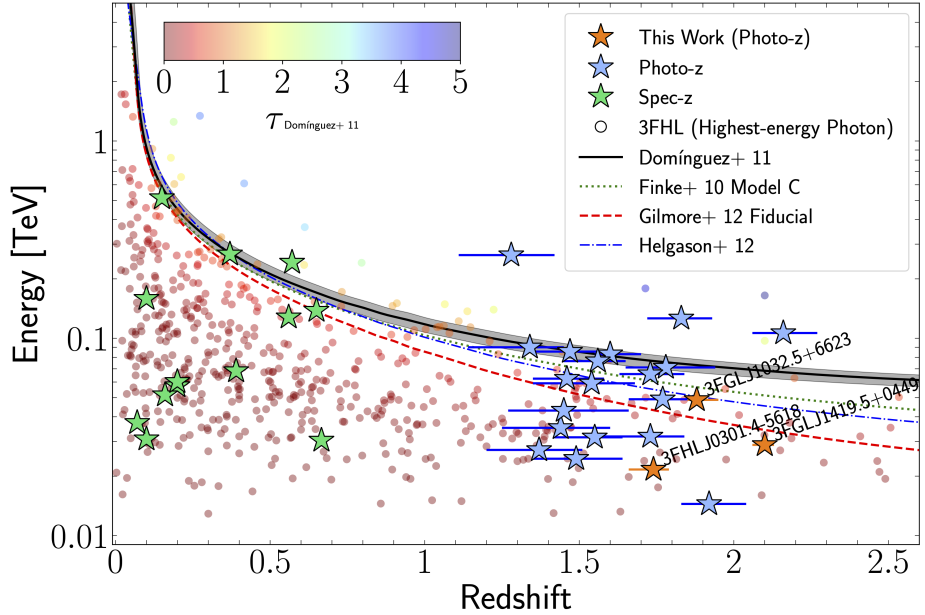


Figure 3. The cosmic gamma-ray horizon plot. The colored circles are from the 3FHL catalog. The color gradient shows optical depth. Lines represent the horizon ($\tau=1$) according to different models from Finke et al. (2010), Gilmore et al. (2012), Helgason & Kashlinsky (2012), and Domínguez et al. (2011). The stars are the sources with determined redshifts from photometric and spectroscopic methods (Marchesi et al. 2018; Desai et al. 2019b; Rajagopal et al. 2021).

All of our sources have $\tau < 1$, which means that they are consistent with the CGRH models developed by Domínguez et al. (2011) and Finke et al. (2010).

The gamma-ray SEDs of the four high- z BL Lacs are shown in Figure 4. We fit the Fermi-LAT Fourth Source Catalog (4FGL, Abdollahi et al. 2020; Lott et al. 2020a) and 3FHL data with a power law attenuated by EBL absorption. The EBL absorption (Domínguez et al. 2011) is applied with a factor $e^{-\tau(E,z)}$ in the fits. The redshift uncertainty determined by the χ^2 fitting is considered in the fits, which is demonstrated by the gray shaded area in the plots. The fits show that redshift uncertainty has a negligible effect on the source flux. Moreover, the effect of redshift uncertainty decreases with higher redshift. In addition, the attenuation caused by the EBL can be seen in the joint fits of the 3FHL and 4FGL data.

6.2. Blazar Sequence

Fossati et al. (1998) introduced the blazar sequence to find a unified model for all types of blazars. The blazar sequence is based on three relations among the physical properties of blazars (Prandini & Ghisellini 2022). The first is an anti-correlation between the rest frame synchrotron peak frequency ($v_{pk, \text{rest}}^{\text{sy}}$) and the luminosity (L_{pk}^{sy}) at this peak frequency. FSRQs occupy the region with lower $v_{pk, \text{rest}}^{\text{sy}}$ and higher L_{pk}^{sy} . On the contrary, BL Lacs show higher $v_{pk, \text{rest}}^{\text{sy}}$ and lower L_{pk}^{sy} . However, this phenomenon could also be ascribed to selection effects (Giommi et al. 2012). BL Lacs with high $v_{pk, \text{rest}}^{\text{sy}}$ and high L_{pk}^{sy} could exist among those that do not have a redshift measurement available. Thus, measuring the redshift of BL Lacs is important to constrain the blazar sequence. The second relation is the anti-correlation between $v_{pk, \text{rest}}^{\text{sy}}$ and Compton dominance. Compton dominance is defined as the ratio of the inverse-Compton peak luminosity (L_{pk}^{IC}) to L_{pk}^{sy} . BL Lacs and FSRQs populate different regions of this plane: FSRQs have higher Compton dominance compared to BL Lacs. The last relation is also an anti-correlation, but it is between the spectral index (Γ_γ) and $v_{pk, \text{rest}}^{\text{sy}}$. They follow similar behavior as the second one mentioned above: FSRQs have larger gamma-ray index and populate lower synchrotron frequencies, while BL Lacs have smaller gamma-ray index and populate higher synchrotron frequencies.

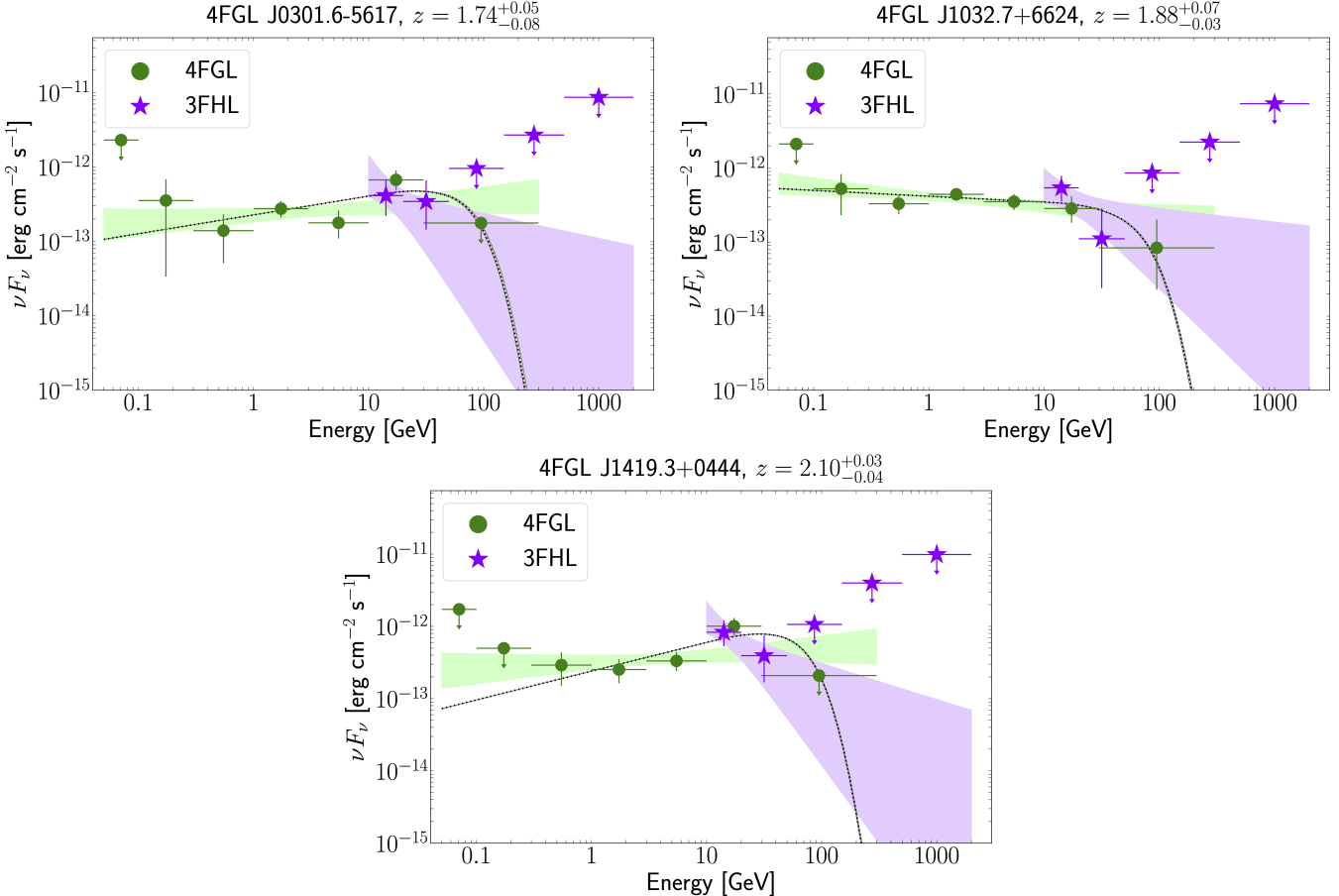


Figure 4. The SED data points are from the 4FGL (green dots) and 3FHL (purple stars) catalogs. The green and purple areas are the power-law fits with 1σ uncertainty provided in the 4FGL and 3FHL catalogs. The green and purple uncertainty bands come from the *Fermi*-LAT data reduction and include statistical uncertainties. The black curves are the best joint power-law fits of 4FGL and 3FHL data attenuated by a factor $e^{-\tau(E,z)}$ due to EBL absorption. The EBL model is taken from Domínguez et al. (2011). The uncertainty region (the grey shaded area) shown for this joint fit is exclusively coming from the redshift uncertainty, according to Domínguez et al. (2011), and the gray area is not easily visible due to the small effects from the redshift uncertainty. The joint fit shows where the energy cutoff is. Note that the energy cutoff is solely due to the EBL attenuation.

In order to explore these relations, we use the SSDC Sky Explorer⁵ to calculate the synchrotron peak frequency and flux of high- z sources if they are not provided in the 4LAC catalog. We also use the equation from Marcotulli et al. (2020) to calculate the inverse Compton peak flux for sources with power-law gamma-ray spectra:

$$\frac{dN}{dE} = K \left[\left(\frac{E}{E_b} \right)^{\delta_1} + \left(\frac{E}{E_b} \right)^{\delta_2} \right]^{-1} \quad (2)$$

The break energy E_b is estimated from the power-law photon index Γ using the $E_b - \Gamma$ relationship reported in Ajello et al. (2015). The normalization constant K is set to reproduce the 1-100 GeV flux reported in the 4FGL catalog. Figure 5(a) shows the existence of high- z luminous BL Lacs that are not detected easily via traditional optical spectroscopy but are discovered by our photometric redshift. On the other hand, in both Figures 5(b) and 5(c), our objects are more in line with the standard regions occupied by BL Lacs.

6.3. The Fermi Blazar Divide

⁵ <https://tools.ssdc.asi.it/>

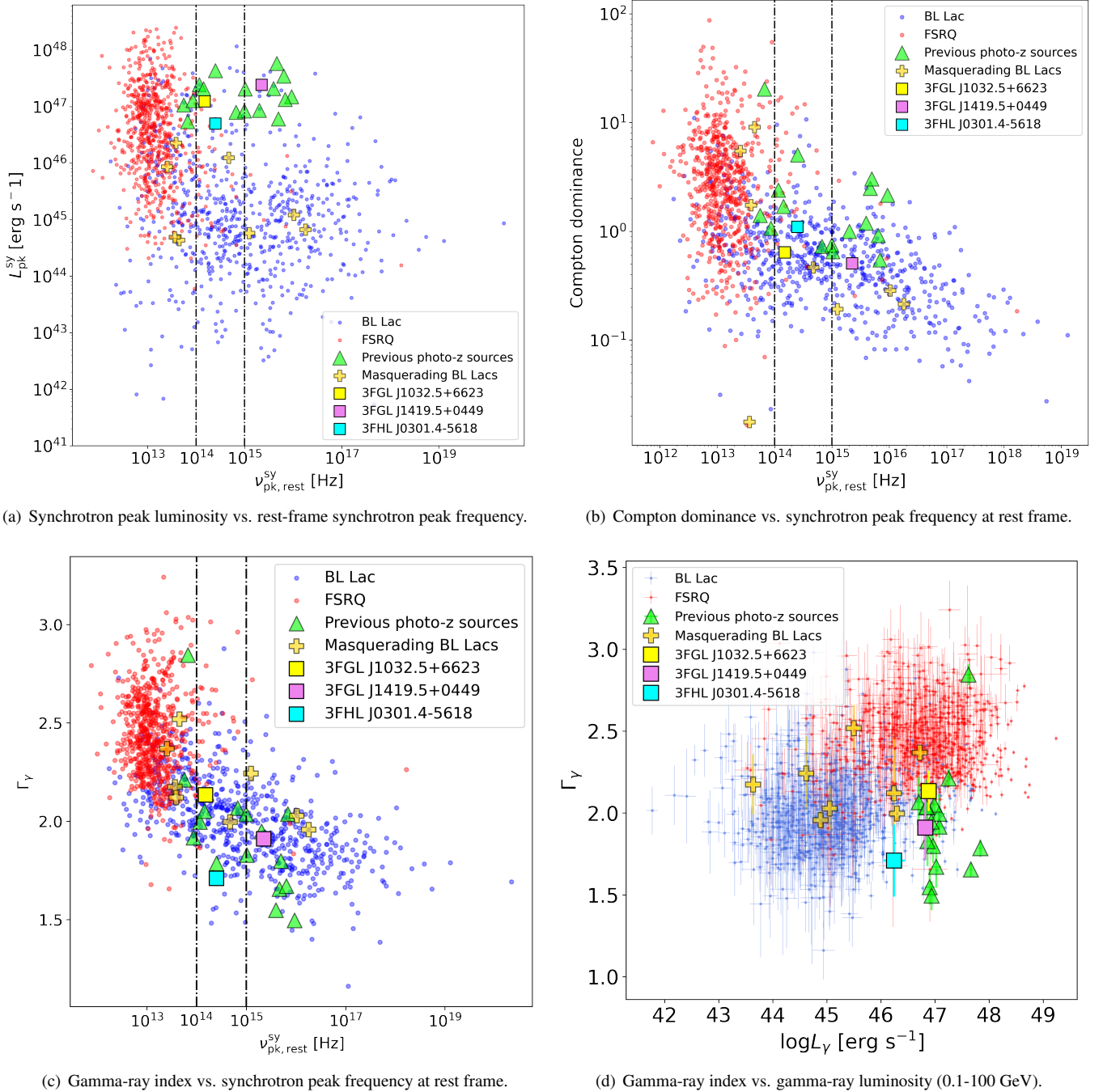


Figure 5. The colored dots are from the 4LAC catalog (Ajello et al. 2020). The triangles represent the sources from previous photo-z papers (Rau et al. 2012; Kaur et al. 2017; Kaur et al. 2018; Rajagopal et al. 2020), while the squares are found in this work. The vertical dotted lines are the divisions for LSP, ISP, and HSP blazars. The orange crosses are the masquerading BL Lacs from Padovani et al. (2022) .Note that the indices are not corrected for EBL absorption.

After three months of Fermi-LAT observations (Abdo et al. 2009), Ghisellini et al. (2009) reported a clear divide between BL Lacs and FSRQs on the gamma-ray index (Γ_{γ}) and gamma-ray luminosity (L_{γ}) plane. BL Lacs are less luminous ($L_{\gamma} < 10^{47}$ erg s $^{-1}$) and have harder spectra ($\Gamma_{\gamma} < 2.2$) than FSRQs. Different accretion rates might account for this phenomenon (Ghisellini et al. 2009). Figure 5(d) reproduces the *Fermi* blazar divide plot using the 4LAC catalog (Ajello et al. 2020) and the high- z sources found by our photometric method. We calculate the gamma-ray luminosity from 0.1 GeV to 100 GeV using equation 1 in Ghisellini et al. (2009). All the high- z sources this paper find have a harder spectrum ($\Gamma_{\gamma} < 2.2$). Although there

is an overlap between BL Lacs and FSRQs, the separation of the two populations is still distinct. However, our BL Lac objects have properties in between FSRQs and BL Lacs (they have high luminosities and hard spectra).

[Giommi et al. \(2013\)](#) proposed that these BL Lacs are “blue quasars” or “masquerading BL Lacs” because the overwhelming synchrotron emission outshines their broad emission lines. According to [Sbarrato et al. \(2012\)](#) the luminosity of the broad line region is connected to the gamma-ray luminosity by $L_{BLR} \sim 4L_\gamma^{0.93}$. On average we assume that 10% of the disk luminosity (L_{disk}) is processed by the broad line region: $L_{BLR} = 0.1L_{disk}$. Then the ratio of L_{disk} to L_{Edd} can be found. For the four high- z sources in this work, the ratios are 0.027, 0.023, and 0.007 for 3FGL J1032.5+6623, 3FGL J1419.5+0449, and 3FHL J0301.4–5618 respectively. Two of the three sources have the ratio between 0.02 to 0.05, suggesting efficient accretion as typical for FSRQs. The overall properties of the BL Lacs with high photometric redshifts ($z > 1.3$) allow us to characterize them as potential masquerading BL Lacs, thus increasing this interesting population.

7. SUMMARY AND CONCLUSIONS

In this work we use 10-filter photometry with *Swift*-UVOT and SARA to constrain the redshift of 60 BL Lac objects without a spectroscopic measurement. Our method, based on the method used in [Rau et al. \(2012\)](#), can produce a photometric redshift measurement for BL Lacs at $z \geq 1.3$ or an upper limit for BL Lacs at lower redshift. Out of the 60 BL Lacs, we discovered 3 new high- z ($z \geq 1.3$) objects and provided upper limits for 41. For the remaining 15 objects, our fits to the photometric data failed to provide an acceptable solution. This work, together with the previous three in this photometric campaign, have discovered a total of 19 BL Lacs with a $z > 1.3$ photometric redshift. Increasing the number of high- z BL Lacs is crucial since they are rare but essential in studying the blazar population and constraining the EBL. Our work shows that these objects have characteristics (high luminosity and high synchrotron peak frequencies) in between those of FSRQs and BL Lacs and that they could belong to the elusive class of ‘masquerading BL Lacs’. Moreover, we find that the photons detected from these objects probe the high- z portion of the CGRH. We also find that the redshift uncertainty has negligible impact on the modeling of the EBL, allowing the use of these newly discovered high- z BL Lacs in future measurements of the EBL.

Y.S. and M.A. acknowledge funding under NASA contracts 80NSSC21K1888 and 80NSSC21K1400. The authors acknowledge the *Swift* team for scheduling all the *Swift*-UVOT observations. They also acknowledge the Southeastern Association for Research in Astronomy for providing SARA-CT and SARA-RM observations. A.D. is thankful for the support of the Ramón y Cajal program from the Spanish MINECO.

Software: Astropy ([Astropy Collaboration et al. 2022](#)), HEASoft (v6.28; [Nasa High Energy Astrophysics Science Archive Research Center \(Heasarc\) 2014](#)), numpy ([Harris et al. 2020](#)), SAO Image DS9 ([Joye & Mandel 2003](#)), Matplotlib ([Hunter 2007](#)), Pandas ([Wes McKinney 2010](#)), Scipy ([Virtanen et al. 2020](#))

REFERENCES

- Abdo, A. A., Ackermann, M., Ajello, M., et al. 2009, The Astrophysical Journal, 700, 597
- Abdo, A. A., Ackermann, M., Agudo, I., et al. 2010, The Astrophysical Journal, 716, 30
- Abdollahi, S., Ackermann, M., Atwood, W., et al. 2018
- Abdollahi, S., Acero, F., Ackermann, M., et al. 2020, The Astrophysical Journal Supplement Series, 247, 33
- Acero, F., Ackermann, M., Ajello, M., et al. 2015, The Astrophysical Journal Supplement Series, 218, 23
- Ackermann, M., Ajello, M., Allafort, A., et al. 2011, The Astrophysical Journal, 743, 171
- . 2012, Science, 338, 1190
- Ajello, M., Romani, R. W., Gasparrini, D., et al. 2013, The Astrophysical Journal, 780, 73
- Ajello, M., Gasparrini, D., Sánchez-Conde, M., et al. 2015, ApJL, 800, L27
- Ajello, M., Atwood, W., Baldini, L., et al. 2017, The Astrophysical Journal Supplement Series, 232, 18
- Ajello, M., Angioni, R., Axelsson, M., et al. 2020, The Astrophysical Journal, 892, 105
- Albareti, F. D., Allende Prieto, C., Almeida, A., et al. 2017, The Astrophysical Journal Supplement Series, 233, 25, aDS Bibcode: 2017ApJS..233..25A
- Arnouts, S., Cristiani, S., Moscardini, L., et al. 1999, Monthly Notices of the Royal Astronomical Society, 310, 540
- Astropy Collaboration, Price-Whelan, A. M., Lim, P. L., et al. 2022, ApJ, 935, 167
- Biteau, J., & Williams, D. A. 2015, The Astrophysical Journal, 812, 60
- Blandford, R. D., & Rees, M. J. 1978, Physica Scripta, 17, 265
- Bohlin, R. C., Colina, L., & Finley, D. S. 1995, The Astronomical Journal, 110, 1316

- Carini, M., Miller, H., Noble, J., & Sadun, A. 1991, *The Astronomical Journal*, 101, 1196
- Chabrier, G., Baraffe, I., Allard, F., & Hauschildt, P. 2000, *The Astrophysical Journal*, 542, 464
- Dermer, C. D., & Schlickeiser, R. 1994, *ApJS*, 90, 945
- Desai, A., Helgason, K., Ajello, M., et al. 2019a, *The Astrophysical Journal Letters*, 874, L7
- Desai, A., Marchesi, S., Rajagopal, M., & Ajello, M. 2019b, *The Astrophysical Journal Supplement Series*, 241, 5
- Domínguez, A., & Ajello, M. 2015, *The Astrophysical Journal*, 813, L34
- Domínguez, A., Finke, J. D., Prada, F., et al. 2013, *The Astrophysical Journal*, 770, 77
- Domínguez, A., Primack, J. R., Rosario, D. J., et al. 2011, *MNRAS*, 410, 2556
- Fabian, A. C. 2008, *AIP Conference Proceedings*, 254, 657
- Finke, J. D., Razzaque, S., & Dermer, C. D. 2010, *ApJ*, 712, 238
- Fossati, G. a., Maraschi, L., Celotti, A., Comastri, A., & Ghisellini, G. 1998, *Monthly Notices of the Royal Astronomical Society*, 299, 433
- Gehrels, N., Chincarini, G., Giommi, P. e., et al. 2004, *The Astrophysical Journal*, 611, 1005
- Ghisellini, G., Maraschi, L., & Tavecchio, F. 2009, *Monthly Notices of the Royal Astronomical Society: Letters*, 396, L105
- Gilmore, R. C., Somerville, R. S., Primack, J. R., & Domínguez, A. 2012, *MNRAS*, 422, 3189
- Giommi, P., Padovani, P., & Polenta, G. 2013, *Monthly Notices of the Royal Astronomical Society*, 431, 1914
- Giommi, P., Padovani, P., Polenta, G., et al. 2012, *Monthly Notices of the Royal Astronomical Society*, 420, 2899
- Greiner, J., Bornemann, W., Clemens, C., et al. 2007, *The ESO Messenger*, 130, 12
- Harris, C. R., Millman, K. J., van der Walt, S. J., et al. 2020, *Nature*, 585, 357
- Helgason, K., & Kashlinsky, A. 2012, *ApJL*, 758, L13
- Hunter, J. D. 2007, *Computing in Science & Engineering*, 9, 90
- Ilbert, O., Arnouts, S., McCracken, H., et al. 2006, *Astronomy & Astrophysics*, 457, 841
- Joffre, S., Silver, R., Rajagopal, M., et al. 2022, *The Astrophysical Journal*, 940, 139
- Joye, W. A., & Mandel, E. 2003, in *Astronomical Society of the Pacific Conference Series*, Vol. 295, *Astronomical Data Analysis Software and Systems XII*, ed. H. E. Payne, R. I. Jedrzejewski, & R. N. Hook, 489
- Kataoka, J., Madejski, G., Sikora, M., et al. 2008, *The Astrophysical Journal*, 672, 787, publisher: American Astronomical Society
- Kaur, A., Rau, A., Ajello, M., et al. 2018, *ApJ*, 859, 80
- Kaur, A., Rau, A., Ajello, M., et al. 2017, *ApJ*, 834, 41
- Keel, W. C., Oswalt, T., Mack, P., et al. 2016, *Publications of the Astronomical Society of the Pacific*, 129, 015002, publisher: IOP Publishing
- Kerby, S., Kaur, A., Falcone, A. D., et al. 2021, *The Astronomical Journal*, 161, 154
- Kröhler, T., Schady, P., Greiner, J., et al. 2011, *A&A*, 526, A153
- Landolt, A. U. 2009, *The Astronomical Journal*, 137, 4186, aDS Bibcode: 2009AJ....137.4186L
- Lott, B., Gasparrini, D., & Ciprini, S. 2020a, doi:10.48550/ARXIV.2010.08406
- . 2020b, arXiv preprint arXiv:2010.08406
- Maraschi, L., Ghisellini, G., & Celotti, A. 1994, 159, 221
- Marchesi, S., Kaur, A., & Ajello, M. 2018, *The Astronomical Journal*, 156, 212
- Marconi, A., Risaliti, G., Gilli, R., et al. 2004, *Monthly Notices of the Royal Astronomical Society*, 351, 169
- Marcotulli, L., Di Mauro, M., & Ajello, M. 2020, *ApJ*, 896, 6
- Marcotulli, L., Paliya, V. S., Ajello, M., et al. 2017, *The Astrophysical Journal*, 839, 96
- Moralejo, A., Domínguez, A., Ramazani, V. F., et al. 2017, arXiv:1709.02238 [astro-ph], arXiv:1709.02238
- Nasa High Energy Astrophysics Science Archive Research Center (Heasarc). 2014, HEAsoft: Unified Release of FTOOLS and XANADU, *Astrophysics Source Code Library*, record ascl:1408.004, ascl:1408.004
- Otero-Santos, J., Acosta-Pulido, J., Becerra González, J., et al. 2022, *Monthly Notices of the Royal Astronomical Society*, 511, 5611
- Padovani, P., & Giommi, P. 1995, *The Astrophysical Journal*, 444, 567
- Padovani, P., Giommi, P., Falomo, R., et al. 2022, *MNRAS*, 510, 2671
- Paiano, S., Falomo, R., Franceschini, A., Treves, A., & Scarpa, R. 2017, *The Astrophysical Journal*, 851, 135
- Perlman, E. S. 2013, in *Planets, Stars and Stellar Systems: Volume 6: Extragalactic Astronomy and Cosmology*, ed. T. D. Oswalt & W. C. Keel (Dordrecht: Springer Netherlands), 305–386
- Pickles, A. 1998, *Publications of the Astronomical Society of the Pacific*, 110, 863
- Poole, T. S., Breeveld, A. A., Page, M. J., et al. 2008, *Monthly Notices of the Royal Astronomical Society*, 383, 627, aDS Bibcode: 2008MNRAS.383..627P
- Prandini, E., & Ghisellini, G. 2022, *Galaxies*, 10, 35
- Racine, R. 1970, *The Astrophysical Journal*, 159, L99
- Rajagopal, M., Kaur, A., Ajello, M., et al. 2020, *The Astrophysical Journal*, 898, 18
- Rajagopal, M., Marchesi, S., Kaur, A., et al. 2021, *The Astrophysical Journal Supplement Series*, 254, 26
- Rau, A., Schady, P., Greiner, J., et al. 2012, *Astronomy & Astrophysics*, 538, A26

- Roming, P. W., Kennedy, T. E., Mason, K. O., et al. 2005, *Space Science Reviews*, 120, 95
- Salvato, M., Hasinger, G., Ilbert, O., et al. 2008, *The Astrophysical Journal*, 690, 1250
- Salvato, M., Ilbert, O., Hasinger, G., et al. 2011, *The Astrophysical Journal*, 742, 61
- Sbarrato, T., Ghisellini, G., Maraschi, L., & Colpi, M. 2012, *MNRAS*, 421, 1764
- Silver, R., Marchesi, S., Marcotulli, L., et al. 2020, *The Astrophysical Journal*, 902, 23
- Smith, J. A., Allam, S. S., Tucker, D. L., et al. 2006
- Stroh, M. C., & Falcone, A. D. 2013, *The Astrophysical Journal Supplement Series*, 207, 28
- Tagliaferri, G., Antonelli, L., Chincarini, G., et al. 2005, *Astronomy & Astrophysics*, 443, L1
- Tody, D. 1986, in *Society of Photo-Optical Instrumentation Engineers (SPIE) Conference Series*, Vol. 627, *Instrumentation in astronomy VI*, ed. D. L. Crawford, 733
- Urry, C. 1993, arXiv preprint astro-ph/9304003
- Urry, C. M., & Padovani, P. 1995, *Publications of the Astronomical Society of the Pacific*, 107, 803
- Virtanen, P., Gommers, R., Oliphant, T. E., et al. 2020, *Nature Methods*, 17, 261
- Wes McKinney. 2010, in *Proceedings of the 9th Python in Science Conference*, ed. Stéfan van der Walt & Jarrod Millman, 56 – 61